Research paper

Isogeometric mindlin-reissner inverse-shell element formulation for complex stiffened shell structures

Yildirim Dirik , Selda Oterkus [*], Erkan Oterkus

Department of Naval Architecture, Ocean and Marine Engineering, University of Strathclyde, Glasgow, United Kingdom

ARTICLE INFO

ABSTRACT

Structural health monitoring (SHM) is a technology that is used to improve the safety, stability, and availability of large engineering structures. One important aspect of SHM is the ability to perform real-time reconstruction of the full-field structural displacements, also known as shape sensing. The inverse Finite Element Method (iFEM) is a technique that has been used for three-dimensional shape sensing of structures using strain data. On the other hand, Isogeometric Analysis (IGA) is a method that utilizes smooth spaces of functions, such as non-uniform rational B-splines, to solve structural problems and has gained significant attention in recent times. In this study, the authors propose a new method for shape sensing of complex stiffened shell structures by combining IGA with the iFEM method. The goal of this research is to accurately reconstruct the complex geometry of the structure without the need for a fine numerical discretization or mesh. To achieve this, the authors have developed an isogeometric Mindlin-Reissner inverse-shell element (IgaiMin) to implement the coupling between IGA and iFEM. The proposed method is validated by solving problems involving simple plates, tee junctions, and partly clamped stiffened panels representing ship structures.

1. Introduction

Marine structures are subjected to harsh environmental conditions which can cause various damage mechanisms such as fatigue damage and corrosion. Such damage scenarios can result in catastrophic consequences such life losses, environmental pollution, and financial losses. Therefore, it is essential to take necessary actions to prevent such problems. One potential solution is utilising shape sensing and structural health monitoring techniques by collecting data from sensors located on the structure, processing this data, and making decisions based on the data. There exist different available approaches for shape sensing and structural health monitoring purposes. Amongst these, inverse Finite Element Method (iFEM) stands for a promising methodology since it doesn't require loading information and can be applicable for monitoring complex structures like marine structures. Moreover, iFEM is fast and it can be applicable for real-time monitoring. There has been a rapid progress on iFEM especially during the recent years. Tessler et al. (Tessler and Spangler, 2004) developed a three-node shell element (iMIN3) and proposed it for structural health monitoring of future aerospace vehicles (Tessler et al., 2011). Other aerospace related applications of iFEM include monitoring of a UAS fixed wing (Papa et al.,

2017), complex aeronautical structure (Oboe et al., 2021), skin antenna structure (Niu et al., 2020), heavy-duty machine tool (Liu et al., 2018), and pipelines (Wang et al., 2021). Gherlone et al. (2012) utilised iFEM for shape sensing of 3-Dimensional frame structures. De Mooij et al. (De Mooij et al., 2019) presented several benchmark problems for solid inverse elements. Kefal et al. (2016) introduced a four-node shell element with drilling degree-of-freedom (iQS4). It has been demonstrated that this element can be applied for monitoring of different marine structures such as chemical tankers (Kefal and Oterkus, 2016a), containerships (Kefal and Oterkus, 2016b), bulk carriers (Kefal et al., 2018a), submarines (Li et al., 2019), and offshore wind turbines (Li et al., 2020a, 2023). iFEM has also been utilised for composite structures (Cerracchio et al., 2015; Kefal et al., 2018b). Damage identification is also possible within iFEM framework (Li et al., 2020b). Another important aspect is determination of optimum sensor locations which is explored in (Kefal et al., 2015). The ability to accurately represent the geometry of a real structure is an essential requirement for iFEM-based shape sensing analysis, especially in the case of curved structures. Flat shell elements such as iQS4 and iMIN3, which use standard polynomial-based shape functions, require a high-fidelity mesh to accurately represent the smooth geometry of a real structure in an iFEM analysis. However, the
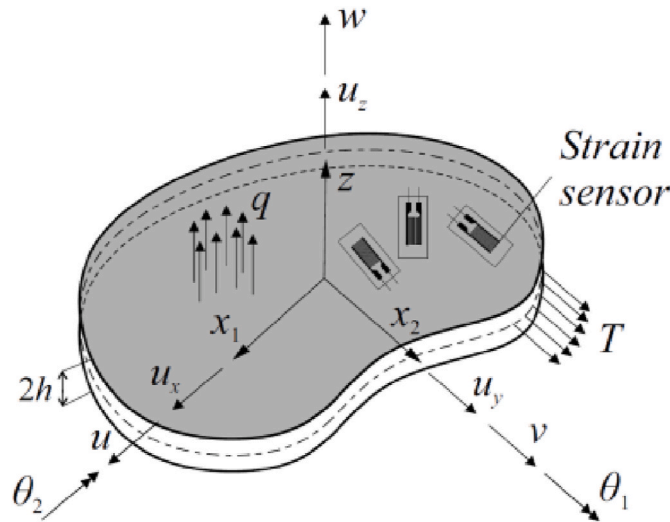
Fig. 1. Shell structure with strain sensors and defined degree-of-freedoms (DoFs) shown on the orthogonal Cartesian Coordinates (Kefal et al., 2016).

generation of such a mesh is a time-consuming and labor-intensive process, and can lead to a need for a large number of strain sensors in the shape sensing analysis. As the number of inverse elements in the iFEM analysis increases, the amount of required measured strain data also increases, which can be impractical in many cases. NURBS basis functions with higher degrees, on the other hand, can provide higher continuity along element and edge interfaces, leading to smoother shape sensing. In order to address these challenges and extend the range of applicability of iFEM, the method of Isogeometric Analysis (IGA) can be employed to create novel isogeometric inverse elements. Besides, by utilising multi-patch framework, IGA can allow for the exact representation of the complex stiffened structures.

For many years, many significant research studies have been published on the topic of NURBS algorithms (Piegl and Tiller, 1995; Rogers, 2001). The concept of isogeometric analysis (IGA) was first introduced by Hughes et al. (2005) as a means of reducing the time and effort required for mesh generation in the field of computational mechanics. IGA has gained significant attention from various fields of computational mechanics, particularly structural and fluid mechanics, due to its potential to greatly improve the efficiency and accuracy of numerical simulations. For instance, Cottrell et al. (2009) provide an overview of IGA and discuss its potential future developments. Additionally, the superiority of IGA over conventional methods has been demonstrated in the field of fluid-structure interaction (FSI) by Bazilevs et al. (2008), and it has also been shown to be effective in other areas such as shell and plate problems (Benson et al., 2010), contact formulations (Temizer et al., 2011), and optimization problems (Wall et al., 2008). Kefal and Oterkus, 2017, 2020 combined IGA and iFEM formulations and introduced the concept of isogeometric iFEM analysis. Following these studies, Zhao et al. (2020) utilised isogeometric iFEM for shape sensing of beam with variable cross-sections. Moreover, Chen et al. (2021) utilised this approach for shape sensing of Timoshenko beam subjected to complex multi-node loads.

This study introduces a new method for performing shape sensing of complex stiffened shell structures using a multi-patch isogeometric inverse finite element method (iFEM) formulation. The aim of this method is to accurately reconstruct the complex geometry of the structure without requiring a fine mesh and to achieve smoother shape sensing even when using fewer strain sensors. To achieve this, the authors have developed an isogeometric Mindlin-Reissner inverse-shell element (IgaiMin) that combines Mindlin-Reissner shell theory with non-uniform rational basis spline (NURBS)-based multi-patch isogeometric analysis. The IgaiMin element makes use of membrane and bending strain

measurements and utilizes NURBS for both discretizing the geometry and performing analysis by using it as a tool for displacement domain discretization. This new element offers several benefits including higher continuity in the shape functions, accurate representation of the real structure, and the ability to use the same computer-aided design (CAD) geometry for both design and analysis. In addition, to the best of the authors' knowledge, this is the first study in the literature to present a multi-patch isogeometric iFEM formulation. The structure of the paper is divided into four parts. The first part discusses the use of Mindlin-Reissner shell theory in orthogonal Cartesian coordinates to develop the multi-patch isogeometric iFEM formulation for flat stiffened shell structures. The second part presents the results of analysing several sample problems, including a simple plate, a tee junction, and a partly clamped stiffened panel, to demonstrate the shape sensing capabilities of the IgaiMin element formulation for multi-patch shells. The final part is a conclusion that summarizes the advantages of the isogeometric iFEM methodology and the IgaiMin element.

2. Methodology: multipatch isogeometric iFEM formulation

In this section, a general overview of multipatch isogeometric iFEM formulation for plate structures is provided. This includes a description of the kinematic relationships of the adopted structural shell theory, the calculation of experimental section strains, and the weighted least squares functional. In addition, the adoption of isogeometric analysis (IGA) for inverse multi-patch applications is discussed, including the isogeometric framework, patch transformations, and the construction of the solution matrix. This overview provides the necessary background information for understanding the development and validation of the novel isogeometric iFEM formulation presented in the following section.

2.1. Inverse problem

The inverse problem is defined on a plate structure with a thickness of 2h which is specified along the z-axis of orthogonal Cartesian co-ordinates as illustrated in Fig. 1. The midplane of the plate structure is considered as located at z = 0 and the strain data is collected from the top and bottom surfaces of the plate by strain sensors as a result of deformation caused by the external in-plane and/or out-of-plane loadings as depicted in Fig. 1. This inverse problem aims to determine the displacement and stress fields in the plate structure from the measured strain data. This information can be used to assess the structural health of the plate and identify any potential damage or defects.

2.2. Shell kinematics

In this study, kinematics of the first order shear deformation theory (FSDT) is used to develop the Isogeometric Inverse Mindlin element (IgaiMin) formulation. The orthogonal components of the displacement vector, u_x, u_y, and u_z, corresponding to any material point within the plate as shown in Fig. 1, can be described in accordance with the FSDT as

$$
\begin{aligned}
u_x(x_1, x_2, z) &= u(x_1, x_2) + z\theta_1(x_1, x_2) \\
u_y(x_1, x_2, z) &= v(x_1, x_2) + z\theta_2(x_1, x_2) \\
u_z(x_1, x_2, z) &= w(x_1, x_2)
\end{aligned}
\tag{1}
$$

where u, v, w, θ_1, and θ_2 are mid-plane displacements and rotations.

2.3. Processing of measured strains

To utilize iFEM, firstly, in situ strain data should be collected by using the strain sensors (rosettes), which are placed at the top, "+", and bottom, "-", sides of the shell (see Fig. 2). Then, the collected strain data are used to calculate the membrane strains, **E**, and bending curvatures, **K**, as:
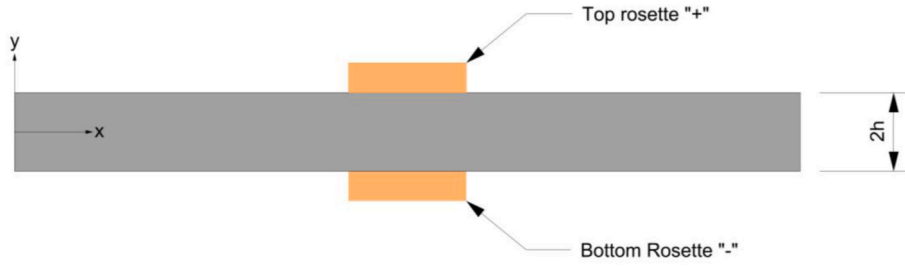
Fig. 2. Rosette placement of the shell structure with the thickness of 2h.

$$\mathbf{E}_i \equiv \begin{Bmatrix} \mathrm{E}_1 \\ \mathrm{E}_2 \\ \mathrm{E}_3 \end{Bmatrix}_i = \frac{1}{2} \begin{Bmatrix} \varepsilon_{11}^+ + \varepsilon_{11}^- \\ \varepsilon_{22}^+ + \varepsilon_{22}^- \\ \gamma_{12}^+ + \gamma_{12}^- \end{Bmatrix}_i \quad (i = 1 - n) \tag{2}$$

$$\mathbf{K}_i \equiv \begin{Bmatrix} \mathrm{K}_4 \\ \mathrm{K}_5 \\ \mathrm{K}_6 \end{Bmatrix}_i = \frac{1}{2h} \begin{Bmatrix} \varepsilon_{11}^+ - \varepsilon_{11}^- \\ \varepsilon_{22}^+ - \varepsilon_{22}^- \\ \gamma_{12}^+ - \gamma_{12}^- \end{Bmatrix}_i \quad (i = 1 - n) \tag{3}$$

$$\mathbf{G}_i \equiv \begin{Bmatrix} G_7 \\ G_8 \end{Bmatrix}_i \quad (i = 1 - n) \tag{4}$$

The number of sensor sets, consisting of top and bottom sensors, is represented by n. Note that transverse shear strains cannot be calculated straightforwardly. However, in marine structures, the majority of the shell structures are thin shells. Therefore, it is possible to make assumption of plane stress condition. For that reason, the transverse shear strains $\mathbf{G}$ can safely be ignored.

2.4. Weighted least squares functional

In this section, a general overview of iFEM is briefly presented. As part of the iFEM methodology, inverse elements are used to discretize the target geometry in the numerical domain to perform structural health monitoring. For each inverse element a least-squares functional Φ^e is created by utilising measured element strains ε_k^e from the actual structure, and analytical element strains ε_k where k indicates the number of independent strain constituents obtained in accordance with the implemented structural theory for the corresponding inverse element as

$$\Phi^e(\mathbf{u}) = \sum_k w_k^e \Phi_k^e \tag{5}$$

where Φ_k^e is defined as

$$\Phi_k^e \equiv \frac{1}{n} \sum_{i=1}^n \left[\varepsilon_{k(i)}(\mathbf{u}^e) - \varepsilon_{k(i)}^e \right]^2 \tag{6}$$

For each inverse element, n number of strain measurements can be used. Weighting coefficients w_k^e helps to eliminate potential issues related with elements with no strain measurement and provide option to emphasize specific independent strain measures. Therefore, the following least-squares functional for the current isogeometric inverse shell element can be written as

$$\Phi(\mathbf{u}) = \sum_{\alpha=1}^8 w_\alpha \, \varphi_\alpha \tag{7}$$

$$\varphi_\alpha \equiv \frac{1}{n} \sum_{i=1}^n \left| e_\alpha(\mathbf{u})_i - E_{\alpha i} \right|^2 \quad (\alpha = 1, 2, 3) \tag{8}$$

$$\varphi_\alpha \equiv \frac{(2h)^2}{n} \sum_{i=1}^n \left| \kappa_\alpha(\mathbf{u})_i - K_{\alpha i} \right|^2 \quad (\alpha = 4, 5, 6) \tag{9}$$

$$\varphi_\alpha \equiv \frac{1}{n} \sum_{i=1}^n \left| g_\alpha(\mathbf{u})_i - G_{\alpha i} \right|^2 \quad (\mathrm{w}_\alpha = \lambda), (\alpha = 7, 8) \tag{10}$$

Furthermore, if an experimentally measured strain component is not available for a particular element, equations will be reduced to L_2 squared norms of only analytical section strains as

$$\varphi_\alpha \equiv \frac{1}{A} \int_A |e_\alpha(\mathbf{u})|^2 dA \quad (\mathrm{w}_\alpha = \lambda), (\alpha = 1, 2, 3) \tag{11}$$

$$\varphi_\alpha \equiv \frac{(2h)^2}{A} \int_A |\kappa_\alpha(\mathbf{u})|^2 dA \quad (\mathrm{w}_\alpha = \lambda), (\alpha = 4, 5, 6) \tag{12}$$

$$\varphi_\alpha \equiv \frac{1}{A} \int_A |g_\alpha(\mathbf{u})|^2 dA \quad (\mathrm{w}_\alpha = \lambda), (\alpha = 7, 8) \tag{13}$$

with the weighting coefficient is set to be a small number, e.g., $\lambda = 10^{-5}$.

2.5. Isogeometric approximation

In this study, non-uniform rational basis spline (NURBS) basis functions are used to model shell structures because they are the most commonly used functions within computer-aided design (CAD) software packages used in industry. Therefore, using NURBS surfaces which are also called NURBS patches, is sufficient for the calculations.

NURBS basis functions are created by utilization of B-spline functions. In 1-D, a NURBS curve is created with a knot vector $\Xi = \{\xi_1, \xi_2, ..., \xi_{m+p+1}\}$ and a vector of control points $\mathbf{C} = \{C_1, C_2, ..., C_m\}$ in which m represents number of control points which is equal to the number of basis functions, and p represents the order of NURBS functions.

When it comes to creating a NURBS patch, linear combination of two-variable NURBS basis functions $R_{ij}^{pq}(\xi, \eta)$ with coordinate matrix $\mathbf{C}_{ij}(\xi, \eta)$ of control points is utilised as

$$\mathbf{S}(\xi, \eta) = \sum_i \sum_j R_{ij}^{pq}(\xi, \eta) \mathbf{C}_{ij} = \sum_i \sum_j \frac{N_{i,p}(\xi) N_{j,q}(\eta) w_{ij}}{\sum_k \sum_l N_{k,p}(\xi) N_{l,q}(\eta) w_{k,l}} \mathbf{C}_{ij} \tag{14}$$

where

$$N_{i,0} = \begin{cases} 1 & \text{if } \xi_i \leq \xi < \xi_{i+1}, \\ 0 & \text{otherwise,} \end{cases} \tag{15}$$

For $p = 1, 2, 3, ...,$ they are defined as

$$N_{i,p}(\xi) = \frac{\xi - \xi_i}{\xi_{i+p} - \xi_i} N_{i,p-1}(\xi) + \frac{\xi_{i+p+1} - \xi}{\xi_{i+p+1} - \xi_{i+1}} N_{i+1,p-1}(\xi) \tag{16}$$

Note that in Eq. (16) it is defined as zero when 0/0 occurs. Hereinafter, in order to prevent any misunderstandings caused by the comma symbol that is traditionally used in subscripts to indicate partial derivatives, the subscript of any B-spline basis function will no longer include the degree p. The B-spline basis functions are positive valued across their entire domain, and a basis function with a degree of p can cover a range of up to $p + 1$ elements.

A NURBS curve $\mathbf{R}(\xi)$ can be defined by associating the control point with the basis function as

$$\mathbf{R}(\xi) = \sum_{i=1}^{N_{cp}} R_i(\xi)\,\mathbf{C}_i \equiv \sum_i R_i(\xi)\,\mathbf{C}_i \tag{17}$$

Note that in Eq. (17), N_{cp} that represents the number of control points is not included when writing the sums that involve basis functions in order to make them more concise.

2.6. Isogeometric inverse shell element

For the isogeometric inverse shell element, the orthogonal components of the mid-surface displacement vector $\mathbf{u}$ is obtained by interpolating the ones of the control points by using NURBS basis functions $R_i(\xi, \eta)$ given in Eq (12) as,

$$\mathbf{u} \equiv \begin{Bmatrix} u \\ v \\ w \\ \theta_1 \\ \theta_2 \end{Bmatrix} = \sum_i R_i(\xi, \eta) \begin{Bmatrix} u_i \\ v_i \\ w_i \\ \theta_{1i} \\ \theta_{2i} \end{Bmatrix} \equiv \sum_i R_i \mathbf{u}_i^e \tag{18}$$

Then the same NURBS basis functions $R_i(\xi, \eta)$ are used for the physical geometry discretization. Strain-displacement relationships can be expressed as:

$$\mathbf{e}(\mathbf{u}) = \begin{Bmatrix} e_1 \\ e_2 \\ e_3 \end{Bmatrix} = \begin{Bmatrix} u_{1,1} \\ u_{2,2} \\ u_{1,2} + u_{2,1} \end{Bmatrix} \tag{19}$$

$$\boldsymbol{\kappa}(\mathbf{u}) = \begin{Bmatrix} \kappa_1 \\ \kappa_2 \\ \kappa_3 \end{Bmatrix} = \begin{Bmatrix} \theta_{1,1} \\ \theta_{2,2} \\ \theta_{1,2} + \theta_{2,1} \end{Bmatrix} \tag{20}$$

$$\mathbf{g}(\mathbf{u}) = \begin{Bmatrix} g_1 \\ g_2 \end{Bmatrix} = \begin{Bmatrix} u_{1,z} + u_{z,1} \\ u_{2,z} + u_{z,2} \end{Bmatrix} = \begin{Bmatrix} w_{,1} + \theta_1 \\ w_{,2} + \theta_2 \end{Bmatrix} \tag{21}$$

By using Eq. (18) strain-displacement relationships can be rewritten as:

$$\boldsymbol{\varepsilon} = \begin{Bmatrix} \boldsymbol{\varepsilon}_m \\ \cdots \\ \boldsymbol{\varepsilon}_b \\ \cdots \\ \boldsymbol{\varepsilon}_s \end{Bmatrix} = \begin{Bmatrix} \dfrac{\partial u}{\partial x_1} \\ \dfrac{\partial v}{\partial x_2} \\ \dfrac{\partial u}{\partial x_2} + \dfrac{\partial v}{\partial x_1} \\ \cdots \\ \dfrac{\partial \theta_1}{\partial x_1} \\ \dfrac{\partial \theta_2}{\partial x_2} \\ \dfrac{\partial \theta_1}{\partial x_2} + \dfrac{\partial \theta_2}{\partial x_1} \\ \cdots \\ \dfrac{\partial w}{\partial x_1} + \theta_1 \\ \dfrac{\partial w}{\partial x_2} + \theta_2 \end{Bmatrix} = \sum_{i=1}^{n} \begin{Bmatrix} \dfrac{\partial R_i}{\partial x_1} u_i \\ \dfrac{\partial R_i}{\partial x_2} v_i \\ \dfrac{\partial R_i}{\partial x_2} u_i + \dfrac{\partial R_i}{\partial x_1} v_i \\ \cdots \\ \dfrac{\partial R_i}{\partial x_1} \theta_{1i} \\ \dfrac{\partial R_i}{\partial x_2} \theta_{2i} \\ \dfrac{\partial R_i}{\partial x_2} \theta_{1i} + \dfrac{\partial R_i}{\partial x_1} \theta_{2i} \\ \cdots \\ \dfrac{\partial R_i}{\partial x_1} w_i + R_i \theta_{1i} \\ \dfrac{\partial R_i}{\partial x_2} w_i + R_i \theta_{2i} \end{Bmatrix} = \sum_i^n \mathbf{B}_i \mathbf{u}_i \tag{22}$$

From Eq. (22) following relationships can be obtained as:

$$\mathbf{e}(\mathbf{u}^e) = \begin{bmatrix} \mathbf{B}_1\,\mathbf{u}^e & \mathbf{B}_2\,\mathbf{u}^e & \mathbf{B}_3\,\mathbf{u}^e \end{bmatrix}^T \tag{23}$$

$$\boldsymbol{\kappa}(\mathbf{u}^e) = \begin{bmatrix} \mathbf{B}_4\,\mathbf{u}^e & \mathbf{B}_5\,\mathbf{u}^e & \mathbf{B}_6\,\mathbf{u}^e \end{bmatrix}^T \tag{24}$$

$$\mathbf{g}(\mathbf{u}^e) = \begin{bmatrix} \mathbf{B}_7\,\mathbf{u}^e & \mathbf{B}_8\,\mathbf{u}^e \end{bmatrix}^T \tag{25}$$

with

$$\mathbf{u}^e = \begin{bmatrix} \mathbf{u}_1^e & \mathbf{u}_2^e & \cdots & \mathbf{u}_{N_{cp}}^e \end{bmatrix}^T \tag{26}$$

$$\mathbf{u}_i^e = \begin{bmatrix} u_i & v_i & w_i \end{bmatrix}^T \left(i = 1 - N_{cp} \right) \tag{27}$$

where the displacement vector $\mathbf{u}^e$ contains translational DOFs of all the control points, and the matrices $\mathbf{B}_\alpha \equiv \mathbf{B}_\alpha(\xi, \eta)$ $(\alpha = 1 - 8)$ are functions of in-plane coordinates (ξ, η) and contain the derivatives of the NURBS basis functions. The explicit form of these matrices can be defined as

$$\mathbf{B}_\alpha = \begin{bmatrix} \mathbf{B}_\alpha^1 & \mathbf{B}_\alpha^2 & \cdots & \mathbf{B}_\alpha^{N_{cp}} \end{bmatrix} \quad (\alpha = 1 - 8) \tag{28}$$

with

$$\mathbf{B}_{mi} = \begin{bmatrix} \dfrac{\partial R_i}{\partial x_1} & 0 & 0 & 0 & 0 \\ 0 & \dfrac{\partial R_i}{\partial x_2} & 0 & 0 & 0 \\ \dfrac{\partial R_i}{\partial x_2} & \dfrac{\partial R_i}{\partial x_1} & 0 & 0 & 0 \end{bmatrix} \tag{29}$$

$$\mathbf{B}_{bi} = \begin{bmatrix} 0 & 0 & 0 & \dfrac{\partial R_i}{\partial x_1} & 0 \\ 0 & 0 & 0 & 0 & \dfrac{\partial R_i}{\partial x_2} \\ 0 & 0 & 0 & \dfrac{\partial R_i}{\partial x_2} & \dfrac{\partial R_i}{\partial x_1} \end{bmatrix} \tag{30}$$

$$\mathbf{B}_{si} = \begin{bmatrix} 0 & 0 & \dfrac{\partial R_i}{\partial x_1} & R_i & 0 \\ 0 & 0 & \dfrac{\partial R_i}{\partial x_2} & 0 & R_i \end{bmatrix} \tag{31}$$

where R is the NURBS basis function, which is utilised as a shape function within the formulation of IgaiMin as a normal practice of application of isogeometric framework on iFEM elements.

Once the strain values are calculated by using Eqs. (2) and (3), the weighted least-squares functional, which previously given in Eq (6) can be established as

$$\Phi_e(\mathbf{u}) = \frac{1}{n} \sum_{i=1}^{n} \left(\sum_{\alpha=1}^{3} w_\alpha \left| e_\alpha(\mathbf{u}^e)_i - E_{\alpha i} \right|^2 + (2h)^2 \sum_{\alpha=4}^{6} w_\alpha \left| k_\alpha(\mathbf{u}^e)_i - K_{\alpha i} \right|^2 \right. \\ \left. + \sum_{\alpha=7}^{8} w_\alpha \left| g_\alpha(\mathbf{u})_i - G_{\alpha i} \right|^2 \right) \tag{32}$$

All strain compatibility relations are explicitly satisfied based on these assumptions, therefore Eq. (6) can be minimized with respect to displacement vector $\mathbf{u}$ of IgaiMin element as

$$\frac{\partial \Phi_e(\mathbf{u}^e)}{\partial \mathbf{u}^e} = \frac{1}{n} \sum_{i=1}^{n} \left(\sum_{\alpha=1}^{3} w_\alpha \frac{\partial \left| e_\alpha(\mathbf{u}^e)_i - E_{\alpha i} \right|^2}{\partial \mathbf{u}^e} + (2h)^2 \sum_{\alpha=4}^{6} w_\alpha \frac{\partial \left| \kappa_\alpha(\mathbf{u}^e)_i - K_{\alpha i} \right|^2}{\partial \mathbf{u}^e} \right. \\ \left. + \sum_{\alpha=7}^{8} w_\alpha \frac{\partial \left| g_\alpha(\mathbf{u}^e)_i - G_{\alpha i} \right|^2}{\partial \mathbf{u}^e} \right) = 0 \tag{33}$$

By substituting Eqs. 29–31, Eq. (33) can be written as

$$\frac{\partial \left| e_\alpha(\mathbf{u}^e)_i - E_{\alpha i} \right|^2}{\partial \mathbf{u}^e} = 2 \left[\mathbf{B}_\alpha(\mathbf{x}_i) \mathbf{u}^e - E_{\alpha i} \right]^T \mathbf{B}_\alpha(\mathbf{x}_i) \quad (\alpha = 1, 2, 3) \tag{34}$$

$$\frac{\partial \left| \kappa_\alpha(\mathbf{u}^e)_i - K_{\alpha i} \right|^2}{\partial \mathbf{u}^e} = 2 \left[\mathbf{B}_\alpha(\mathbf{x}_i) \mathbf{u}^e - K_{\alpha i} \right]^T \mathbf{B}_\alpha(\mathbf{x}_i) \quad (\alpha = 4, 5, 6) \tag{35}$$
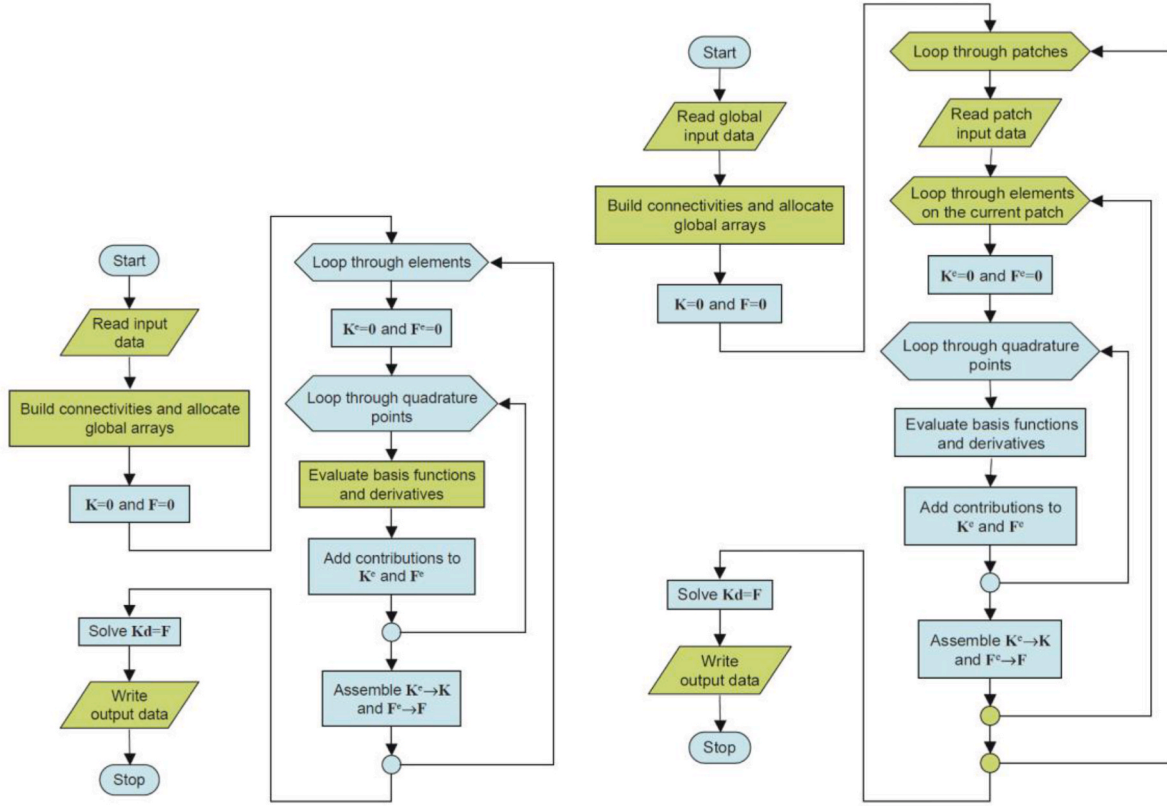
Fig. 3. Flow-charts of single-patch (left) and multi-patch (right) analyses (Cottrell et al., 2009).

$$\frac{\partial \left| e_a(\mathbf{u}^e)_i - G_{ai} \right|^2}{\partial \mathbf{u}^e} = 2[\mathbf{B}_a(\mathbf{x}_i)\mathbf{u}^e - G_{ai}]^T \mathbf{B}_a(\mathbf{x}_i) \quad (\alpha = 7, 8) \tag{36}$$

$$\frac{\partial \Phi_e(\mathbf{u}^e)}{\partial \mathbf{u}^e} = 2(\mathbf{K}^e \mathbf{u}^e - \boldsymbol{\varepsilon}^e) = 0 \tag{37}$$

$$\mathbf{K}^e \mathbf{u}^e = \boldsymbol{\varepsilon}^e \tag{38}$$

where $\mathbf{K}^e$ and $\boldsymbol{\varepsilon}^e$ are the left-hand-side matrix and strain vector for an IgaiMin element, which can explicitly be calculated as

$$\mathbf{K}^e = \frac{1}{n} \sum_1^n \left(\sum_{a=1}^3 \left[w_a [\mathbf{B}_a(\mathbf{x}_i)]^T \mathbf{B}_a(\mathbf{x}_i) \right] + (2h)^2 \sum_{a=4}^6 \left[w_a [\mathbf{B}_a(\mathbf{x}_i)]^T \mathbf{B}_a(\mathbf{x}_i) \right] \right. $$
$$\left. + \sum_{a=7}^8 \left[w_a [\mathbf{B}_a(\mathbf{x}_i)]^T \mathbf{B}_a(\mathbf{x}_i) \right] \right) \tag{39}$$

$$\boldsymbol{\varepsilon}^e = \frac{1}{n} \sum_1^n \left(\sum_{a=1}^3 \left[w_a [\mathbf{B}_a(\mathbf{x}_i)]^T E_{ai} \right] + (2h)^2 \sum_{a=4}^6 \left[w_a [\mathbf{B}_a(\mathbf{x}_i)]^T K_{ai} \right] \right.$$
$$\left. + \sum_{a=7}^8 \left[w_a [\mathbf{B}_a(\mathbf{x}_i)]^T G_{ai} \right] \right) \tag{40}$$

2.7. Multi-patch inverse isogeometric framework

When the target structure involves combination of multiple intersections, modelling it by using a single NURBS patch becomes highly cumbersome or impossible. For such problems, utilization of multiple patches within the numerical domain, i.e. multi-patch assembly, is essential.

In the multipatch framework, the analysis procedure involves an additional level of calculation targeting the assembly of the patches which can involve multiple inverse isogeometric elements individually.

For each patch, a specific input data is read to construct the inverse isogeometric elements for the particular patch. After creating the patches with their elements, an assembly process is followed (see Fig. 3). During that assembly process, the patches are seamlessly connected at their interfaces, allowing for higher continuity and improved accuracy in the analysis. This is achieved by using matching degrees of freedom at the interfaces between patches, which ensures that the displacement and stress fields are continuous across the patches. Additionally, the use of higher-order basis functions allows for higher continuity along the element and edge interfaces, further improving the accuracy of the analysis.

To achieve a seamless connection between the patches created by using IgaiMin elements, the degrees of freedom need to be matching at the conjunctions. However, the FSDT based formulation of IgaiMin element provides 5 DoF solution without drilling DoF for each control point of the patch. This creates a problem when the patch normals are in different directions in 3-D space. To solve this problem, IgaiMin element involves a sixth degree of freedom with the extension of stiffness matrix and related vectors. Within this procedure, an arbitrary coefficient is inserted to patch stiffness matrix as suggested by Oñate et al. (Oñate, 2013) to avoid the singularity problem as shown below:

$$\mathbf{K}_{ij} = \begin{bmatrix} \mathbf{K}_{ij}^e & 0 \\ 0 & \mathbf{K}_{\theta z} \end{bmatrix} \tag{41}$$

where $\mathbf{K}_{\theta z}$ is selected on the order of $2hA^e 10^{11}$ where h is the half thickness of the shell and A^e is the area of the element. This approach is adopted from (Oñate, 2013) for iFEM based approach, and it is determined that the selected arbitrary value of $\mathbf{K}_{\theta z}$ has no observable effect on the analysis results as long as it is selected other than zero.

2.8. Isogeometric flat patch transformation

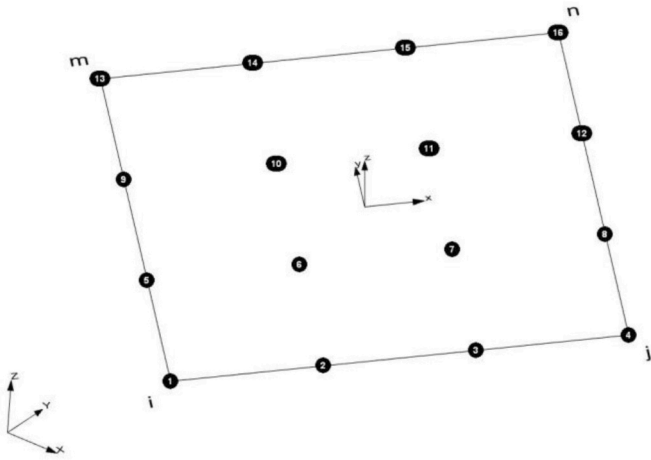The patch transformation maps the coordinates of a point in one

Fig. 4. Control point numbering and identified corner control points of the patch, which involves one 3rd order (in both directions) flat isogeometric shell element.
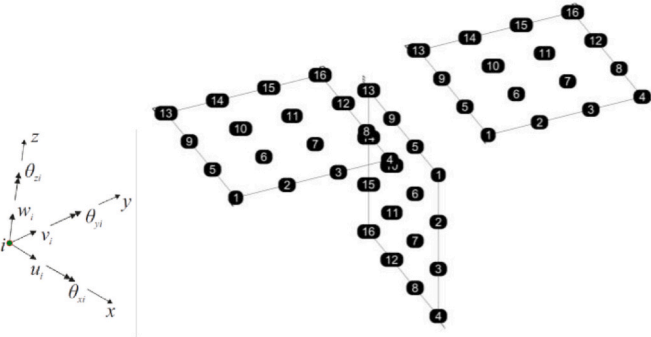

Fig. 5. Control point DoFs corresponding to the local patch coordinates (x, y, z).

patch to the coordinates of the corresponding point in another patch. This allows for the seamless connection of the patches at their interfaces, ensuring that the displacement and stress fields are continuous across the patches. The patch transformation is typically defined using a combination of translation, rotation, and scaling transformations, which can be used to align the patches with one another and match their degrees of freedom at the interfaces.

Since patches utilised within our inverse isogeometric framework are flat, the first step is to obtain the local patch coordinate system (x, y, z) relative to the global coordinate system (X, Y, Z). Corner control points of the patch are required to be identified, as shown in Fig. 4.

In the following procedure, the indices numbering $(1 - 4)$ corresponds to the corner control points in the order $i, j, n, m,$ respectively.

$$\mathbf{X}_i = [X_i \quad Y_i \quad Z_i]^T \ (i = 1 - 4) \tag{42}$$

Each patch edge length d_i and the global coordinates of patch edge mid-points $\mathbf{c}_i$ can be calculated as

$$d_i = \|\mathbf{x}_j - \mathbf{x}_i\| \tag{43}$$

$$\mathbf{c}_i = \frac{(\mathbf{x}_j - \mathbf{x}_i)}{2} \tag{44}$$

$$(i = 1, 2, 3, 4; j = 2, 3, 4, 1) \tag{45}$$

The global coordinates of the patch centroid can be calculated as

$$\mathbf{C} = \frac{\sum_{k=1}^{4} c_k d_k}{\sum_{k=1}^{4} d_k} \tag{46}$$

Unit normal vector to plane (along local z) $\mathbf{n}$ and unit vectors along local y- and x-axes, $\mathbf{p}$ and $\mathbf{l}$, can respectively be computed as

$$\mathbf{n} = \frac{\mathbf{A} \times \mathbf{B}}{\|\mathbf{A} \times \mathbf{B}\|}, \tag{47}$$

$$\mathbf{p} = \frac{\mathbf{A} + \mathbf{B}}{\|\mathbf{A} + \mathbf{B}\|}, \tag{48}$$

$$\mathbf{l} = \mathbf{p} \times \mathbf{n} \tag{49}$$

where

$$\mathbf{T} = [\mathbf{l}^T \quad \mathbf{p}^T \quad \mathbf{n}^T] \tag{50}$$

$$\mathbf{A} = \mathbf{x}_3 - \mathbf{x}_1 \tag{51}$$

$$\mathbf{B} = \mathbf{x}_4 - \mathbf{x}_2 \tag{52}$$

are diagonal vectors with $\mathbf{A}$ pointing out from control point i to n, whereas $\mathbf{B}$ pointing out from control point j to m. Local coordinates of the control points within the patch can be calculated as

$$x_i = (\mathbf{X}_i - \mathbf{C}) \cdot \mathbf{l} \tag{53}$$

$$y_i = (\mathbf{X}_i - \mathbf{C}) \cdot \mathbf{p} \tag{54}$$

$(i = 1, 2, 3 \ldots \#$ of control points in the patch$)$

The transformation matrix for the patch $\mathbf{T}^p$ can be defined as

$$\mathbf{T}^p = \begin{bmatrix} \mathbf{T} & \cdots & \mathbf{T} \\ \vdots & \ddots & \vdots \\ \mathbf{T} & \cdots & \mathbf{T} \end{bmatrix} \tag{55}$$

where

$$\mathbf{T} = [\mathbf{l}^T \quad \mathbf{p}^T \quad \mathbf{n}^T] \tag{56}$$

The size of $\mathbf{T}^p$ is determined according to the number of control points within the patch suitably that each control point has 6-DoF to be transformed as shown in Fig. 5. For example, the required transformation matrix for a patch with 16 control points (see Fig. 5) is calculated as a 96 by 96 matrix with 32 $\mathbf{T}$ submatrices in the diagonal.

3. Numerical examples

In the following section, the application and validation of the IgaiMin element is demonstrated through the analysis of three numerical examples. The first two examples, a simple plate and a Tee junction, are used to show that the IgaiMin element is functional for problems involving membrane and bending for both single and multi-patch frameworks. The third example, a stiffened panel problem representing a ship structure, is used to further investigate the capabilities of the IgaiMin element in providing accurate results for complex structures involving intersecting members. This problem is commonly used in the study of shell elements because it exposes the element to various complex stress states. By demonstrating the effectiveness of the IgaiMin element in these examples, the validity of its use in inverse finite element analysis of shell structures is demonstrated.

3.1. Single patch geometry

The IgaiFEM analysis presented in this example involves a simple plate with dimensions of 1x1x0.01m and material properties of Elastic modulus, E = 210 GPa and Poisson's ratio, v = 0.3. The plate is discretized using iFEM discretization of 2x2, 3x3, and 4x4 IgaiMin elements, and one set of sensors is assigned to each element. The plate is subjected to four different loading scenarios, including membrane tensile loading, membrane shear loading, transverse bending loading, and
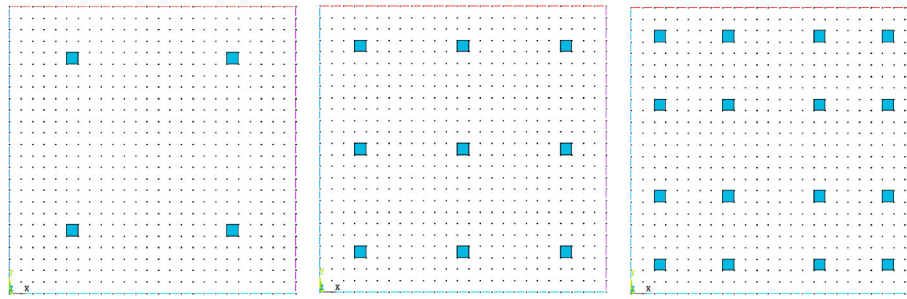
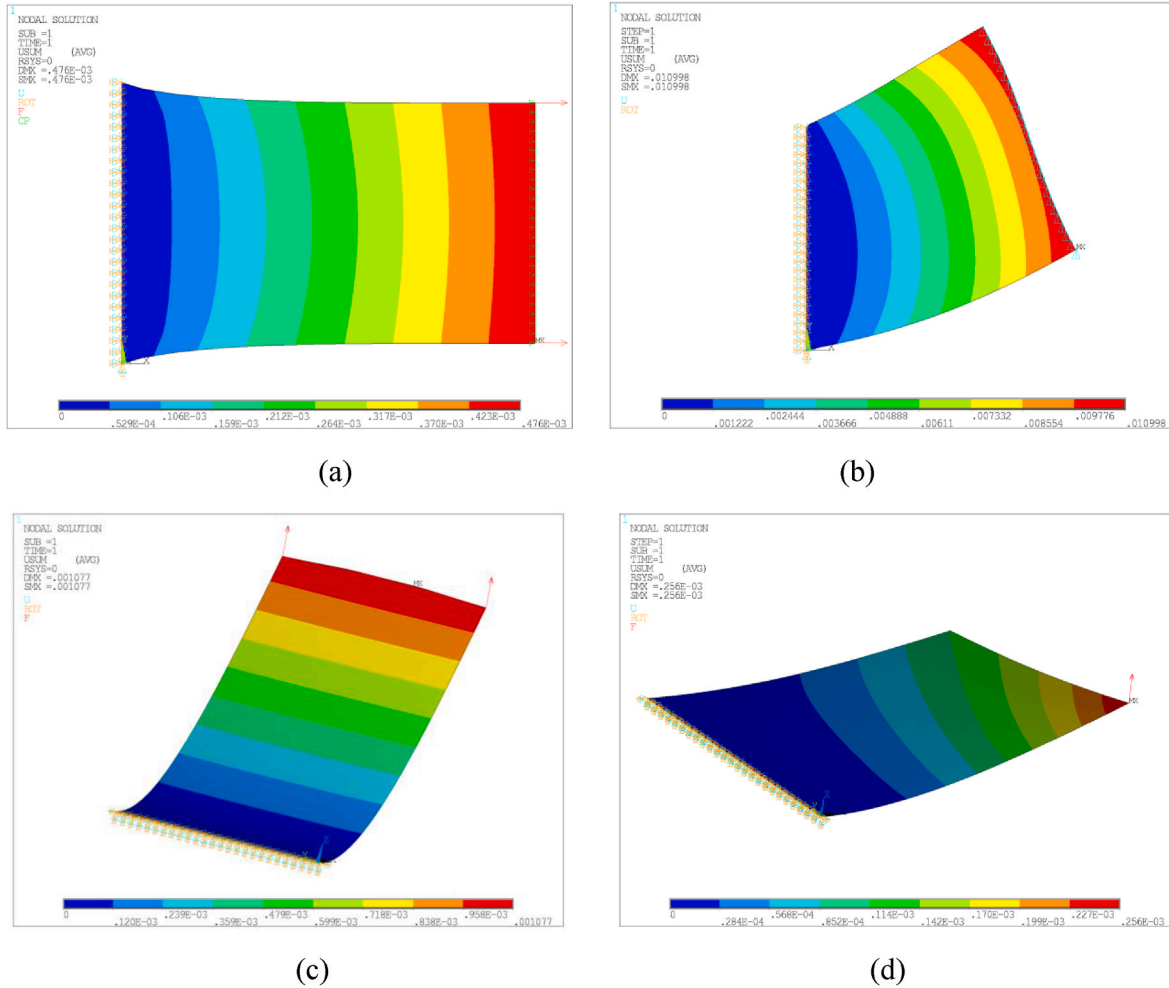**Fig. 6.** Placement of rosettes on the structure.

(a)

(b)

(c)

(d)

Fig. 7. FEM total displacement results for (a) the tensile loading case, (b) the membrane shear loading case, (c) the transverse bending loading case, (d) the asymmetrical transverse loading case.

asymmetrical loading for torsional bending effect. For all cases the left edge of the plate is fixed.

For each inverse element, synthetic strain data is obtained (see Fig. 6) from the finite element analysis (FEA) model with 625 elements and NURBS shape functions' polynomial degrees p and q are set as 6. Therefore, for each element, two strain gauges are placed on the top and bottom surfaces. The maximum displacement values acquired by using the high-fidelity FEM analysis of the structure are given in Fig. 7a–d.

The first scenario, i.e. membrane tensile loading, involves a structure subjected to a distributed tensile force of 1 MN applied at the right edge as shown in Fig. 7a. The maximum deformation is 0.0000476 m. The percentage errors for IgaiMin are 2.18% for a 2x2 grid, 0.06% for a 3x3

grid, and 0.13% for a 4x4 grid (see Fig. 8). For the traditional iFEM element iQS4 (Kefal et al., 2016), the errors are 2.53% for a 2x2 grid, 0.87% for a 3x3 grid, and 0.46% for a 4x4 grid. iQS4 results are not given for conciseness of the paper. In this case, IgaiMin generally outperforms iQS4, particularly for the 3x3 and 4x4 grid sizes.

In the second scenario, i.e. membrane shear loading, a displacement boundary condition of 0.010 m is set at the right edge as shown in Fig. 7b. The maximum deformation reaches 0.011 m. The percentage errors for IgaiMin are 18.22% for a 2x2 grid, 5.22% for a 3x3 grid, and 0.49% for a 4x4 grid (see Fig. 9). For IQS4, the errors are 17.94% for a 2x2 grid, 5.62% for a 3x3 grid, and 0.99% for a 4x4 grid. In this case, both methods have similar percentage errors.
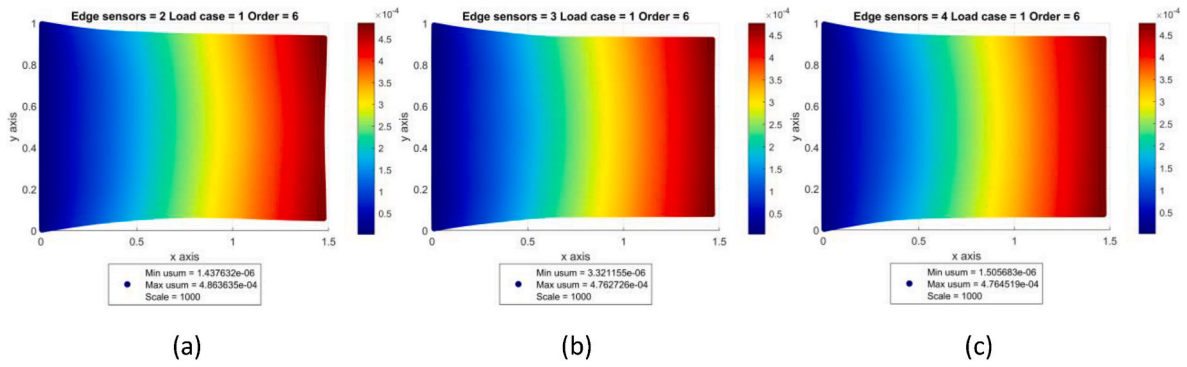
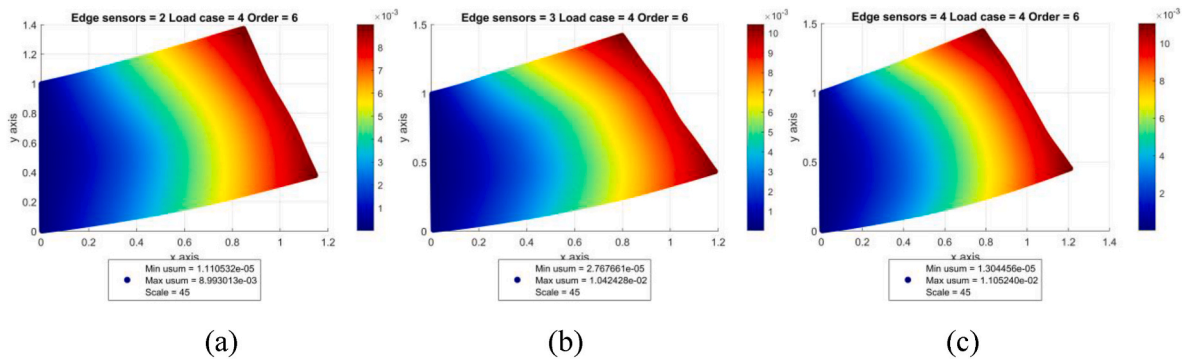**Fig. 8.** Total displacement result for the tensile loading case.

Fig. 9. Total displacement result for the membrane shear loading case.

For the transverse bending loading scenario, the structure is fixed from the left edge, and a distributed transverse force of 60N is applied at the right edge (see Fig. 7c), resulting in a maximum deformation of 0.0011 m. The percentage errors for IgaiMin are 5.30% for a 2x2 grid,

2.17% for a 3x3 grid, and 0.89% for a 4x4 grid (see Fig. 10). For IQS4, the errors are 4.71% for a 2x2 grid, 2.02% for a 3x3 grid, and 1.41% for a 4x4 grid.

Lastly, the fourth scenario features asymmetrical loading for the
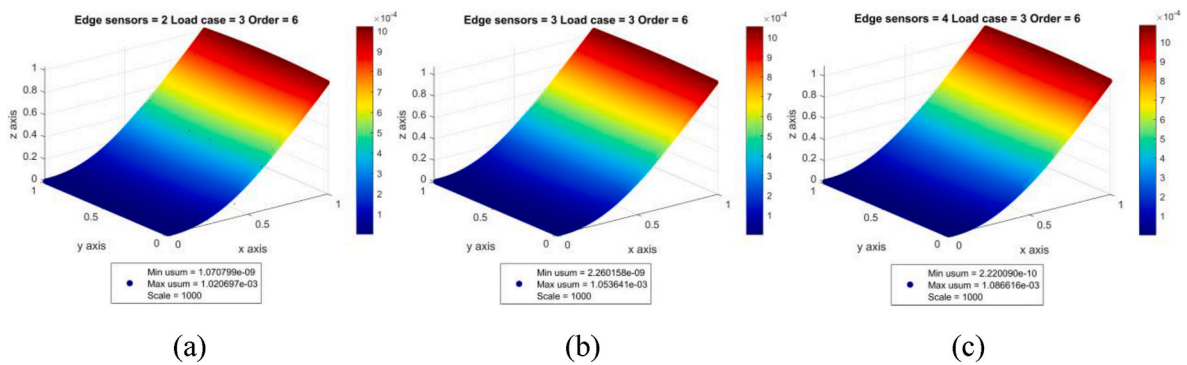
Fig. 10. Total displacement result for the transverse bending loading case.
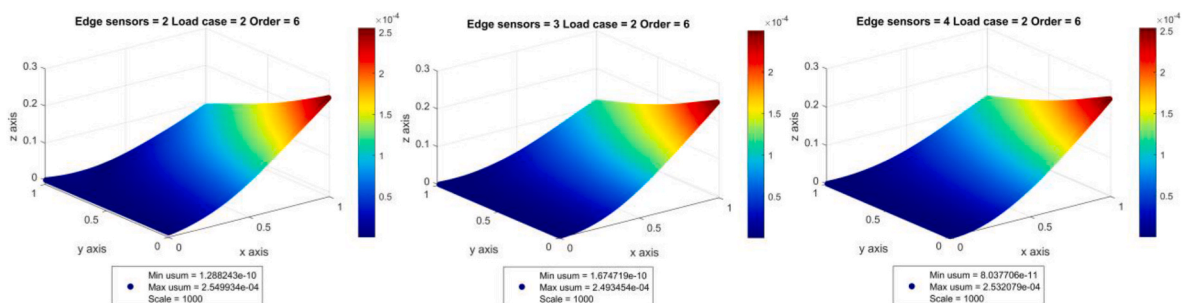
Fig. 11. Total displacement result for the asymmetrical transverse loading case.
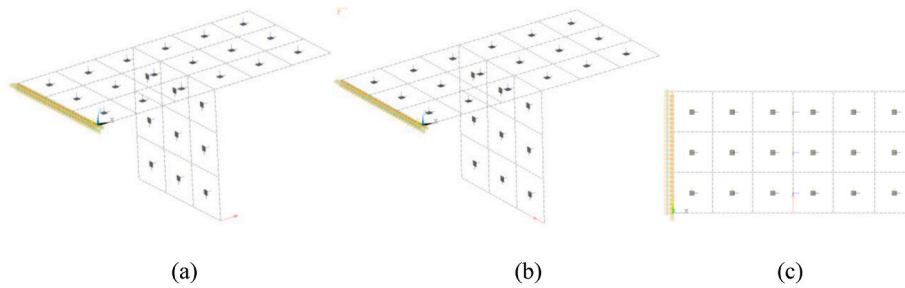
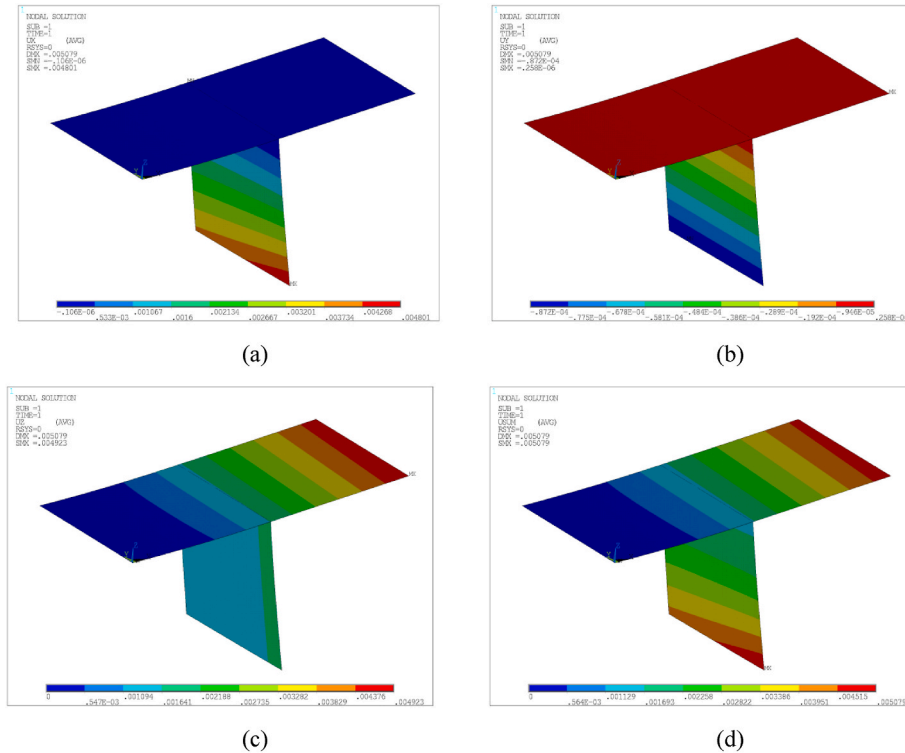**Fig. 12.** Sensor placement and the loading condition for (a) Case 1, (b) and (c) Case 2.

Fig. 13. FEM displacements for Case 1: (a) along x-axis (*u*), (b) along y-axis (*v*), (c) along z-axis (*w*), (d) total displacement.

torsional bending effect (see Fig. 7b). The membrane is fixed from the left edge, and a point transverse force of 10 N is applied at the right bottom corner. The maximum deformation is 0.000256 m. The percentage errors for IgaiMin are 0.39% for a 2x2 grid, 2.60% for a 3x3 grid, and 1.09% for a 4x4 grid (see Fig. 11). For IQS4, the errors are 0.60% for a 2x2 grid, 0.34% for a 3x3 grid, and 0.20% for a 4x4 grid.

3.2. Multi patch tee geometry

In this iFEM analysis, three different discretization cases are considered by dividing the edges of the structure by 3 IgaiMin elements. NURBS shape functions' polynomial degrees *p* and *q* are set as 3 and C1-continuity is provided along each one of the models. The target structure consists of three 10 mm thick plates with dimensions of 1 × 1 m. The inverse model is discretized into 27 patches, each consisting of 27 third-order IgaiMin elements and each of them is fed with a strain data collected from the FEM model representing a sensor set consists of two strain rosettes at both sides of the shell structure. The elastic modulus of the material used in the model is E = 210 GPa, and the Poisson ratio is *ν*

= 0.3. The left edge of the model is fixed.

In the first scenario, Case 1, the structure is subjected to bending loading with a point load of 60 kN as depicted in Fig. 12a iFEM and reference FEM results are given in Figs. 13 and 14. The percentage errors for IgaiMin shape sensing in this case are as follows: 1.92% for *u*, 0.16% for, *v*, and 0.64% for *w*.

In the second scenario, Case 2, the structure undergoes torsional loading with a point load of 60 kN as illustrated in Fig. 12b iFEM and reference FEM results are given in Figs. 15 and 16. The percentage errors for IgaiMin shape sensing in this case are: 0.54% for *u*, 6.01% for *v*, and 2.58% for *w*.

3.3. Multi patch stiffened panel geometry

To demonstrate the applicability of IgaiMin element for ship structures, the stiffened panel design given by Ming Cai et al. (Xu and Guedes Soares, 2013) is investigated in this section (see Fig. 17). The material properties are decided to be chosen for a realistic marine SHM case to be established. Therefore, the material is chosen as EH36 with elastic
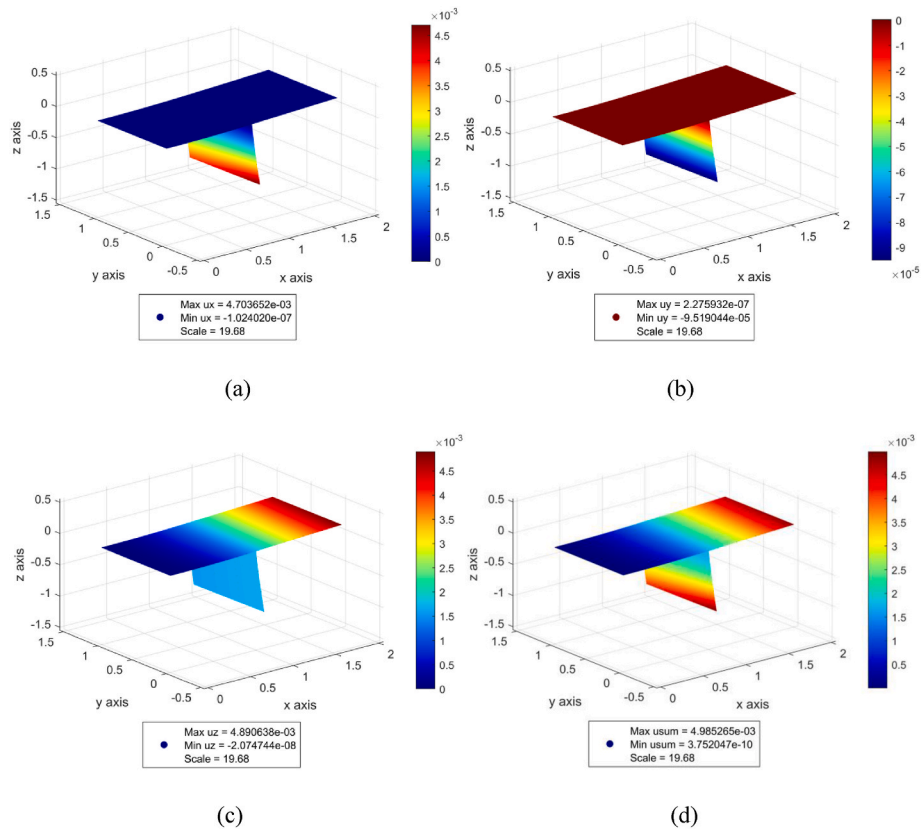
Fig. 14. IgaiMin displacements for Case 1: (a) along x-axis (***u***), (b) along y-axis (***v***), (c) along z-axis (***w***), (d) total displacement.

Fig. 15. FEM displacements for Case 2: (a) along x-axis (***u***), (b) along y-axis (***v***), (c) along z-axis (***w***), (d) total displacement.
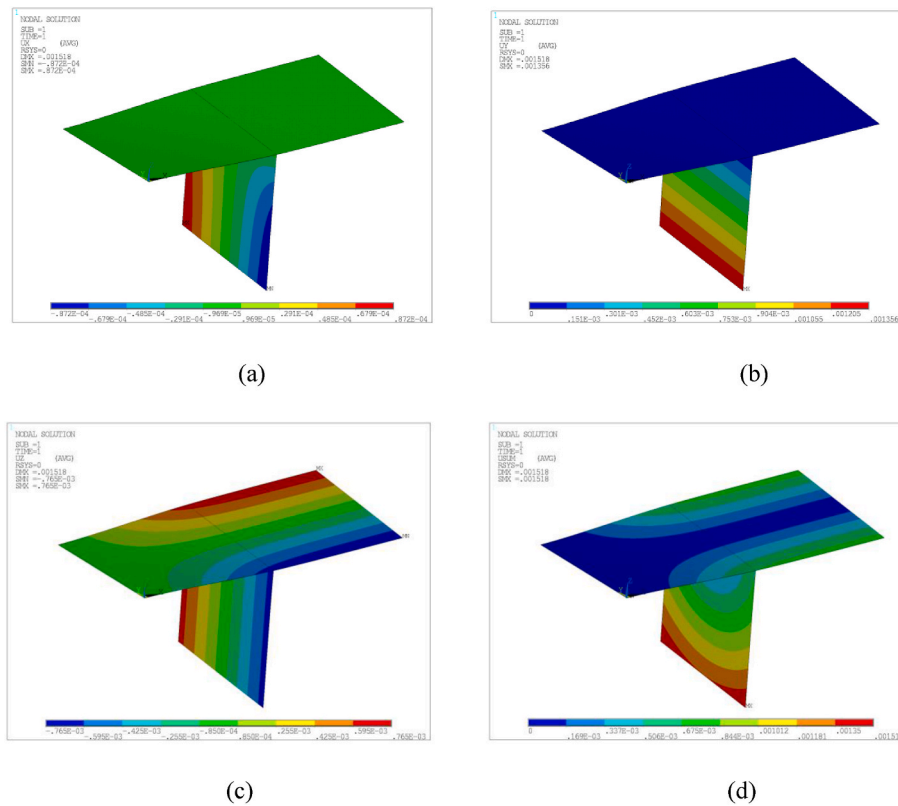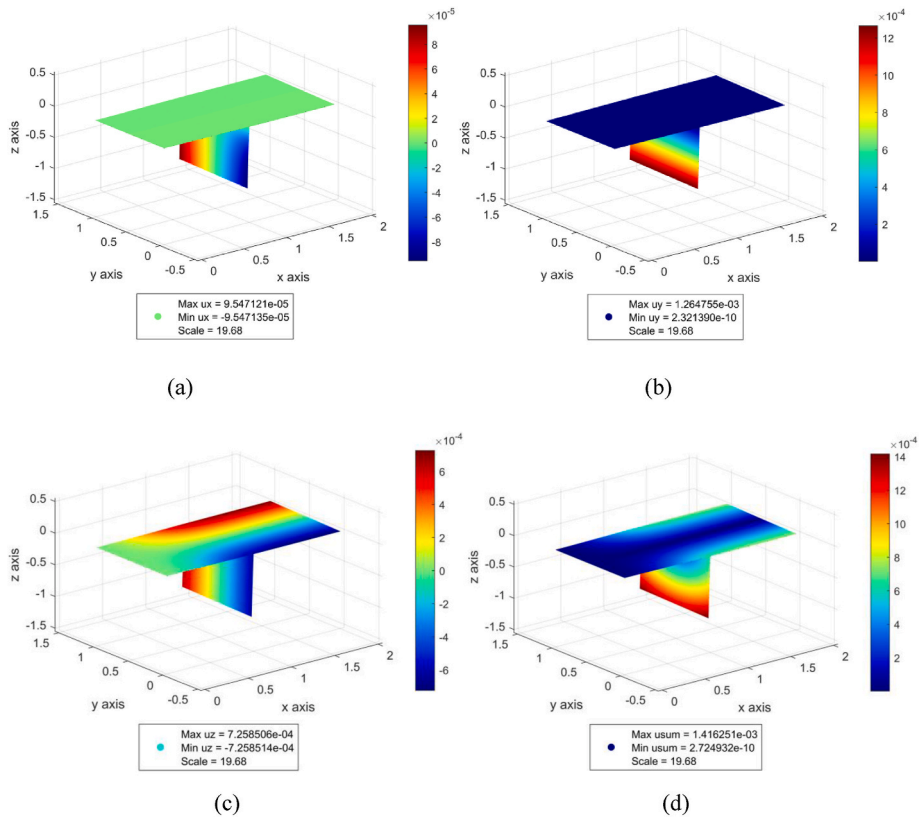
Fig. 16. IgaiMin displacements for Case 2: (a) along x-axis (*u*), (b) along y-axis (*v*), (c) along z-axis (*w*), (d) total displacement.
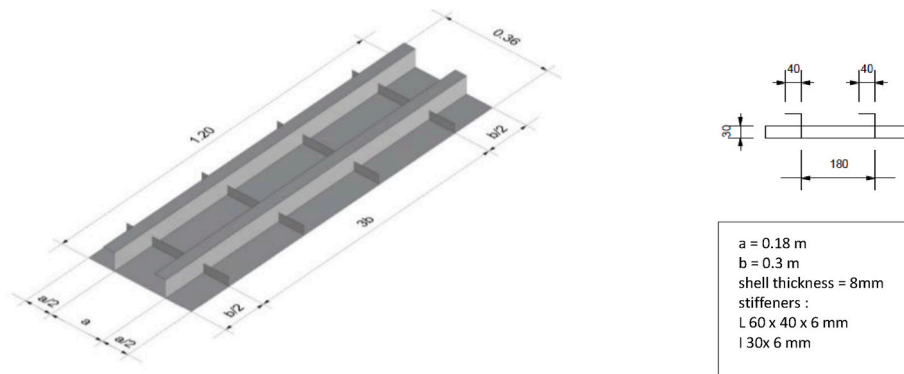

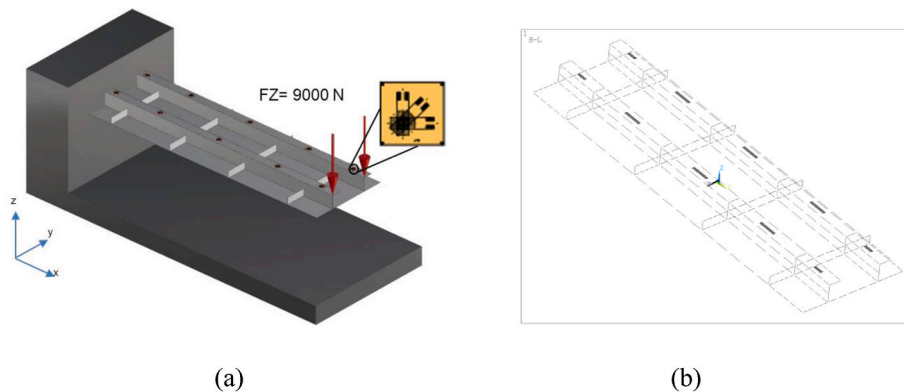**Fig. 17.** Dimensions of the stiffened panel.

Fig. 18. (a) Clamped boundary condition and the applied load on the structure (b) synthetic strain locations from the FEM model.
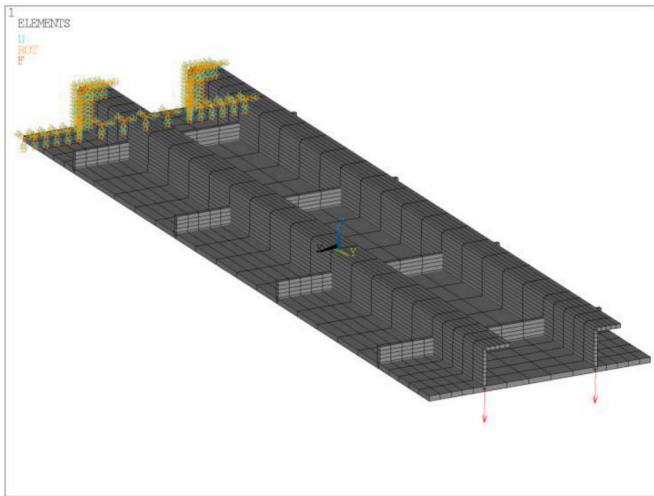
11

Fig. 19. FEM model of the structure.

modulus of 210 GPa and Poisson's Ratio of 0.3. The loading scenario is chosen as cantilever bending case after application of 9 kN of vertical loading from one end as shown in Fig. 18a. By applying such loading, the resulting deformation of the structure involves torsion in addition to a global bending, since the problem is not symmetrical, and it makes the problem more complicated compared to a simple bending scenario.

The structure is divided by 57 IgaiMin elements. NURBS shape functions' polynomial degrees p and q are set as 5 and C1-continuity is provided along each one of the models. Furthermore, unlike in the previous problem, a practical scenario is considered for sensor placement. Hence, 10 of 57 inverse elements are subjected to strain data

provider to perform shape sensing analysis. The strain data is generated by performing FEA with a fine mesh model as given in Fig. 19. The total number of finite elements is 1425 in the FEA model. The locations of the sensors are chosen such that the sensor are placed only on the flange parts of the structural members as shown in Fig. 18b. Therefore, the base plate which may represent the outer shell of the hull will not have strain rosettes which can be exposed to harsh marine conditions. For each of those 10 elements, two strain gauges are placed. The maximum displacement values acquired by using the high-fidelity FEM analysis, iFEM analyses of the structure by using IgaiMin and IQS4 are given in Figs. 20–22, respectively. The percentage errors for IgaiMin shape sensing in this case are: 1.87% for *u*, 0.70% for *v*, 0.20% for *w*, and 0.22 for total displacement. However, for IQS4 element the errors are 7.31% for *u*, 0.27% for *v*, 2.49% for *w*, and 2.38% for total displacement.

4. Conclusions

In this study, a new isogeometric Mindlin-Reissner inverse-shell element (IgaiMin) that combines Mindlin-Reissner shell theory with NURBS-based multi-patch isogeometric analysis is introduced as part of a new method for shape sensing analysis of complex stiffened structures. This new element demonstrated its effectiveness on shape sensing and benefits of utilization higher continuity in the shape functions, accurate representation of the real structure, and the ability to use the same computer-aided design (CAD) geometry for both design and analysis. By solving several sample problems, including a simple plate, a tee junction, and a partly clamped stiffened panel, and by making comparisons of the results achieved using newly developed IgaiMin and IQS4 demonstrate the shape sensing capabilities of the IgaiMin element formulation for multi-patch shells.
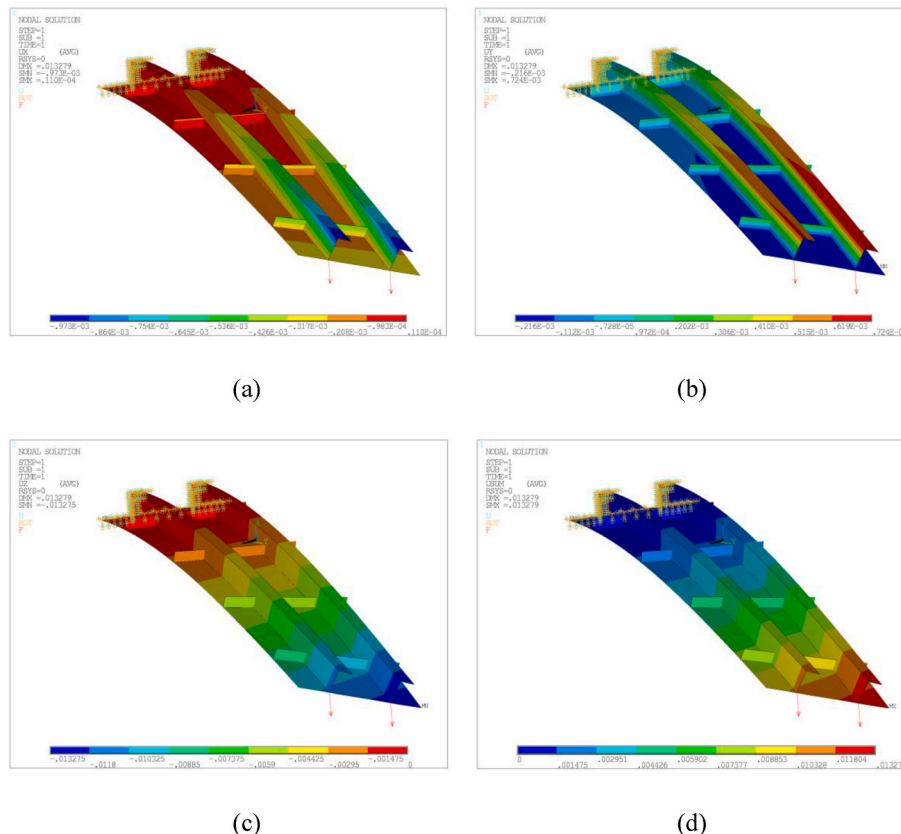

(a)

(b)

(c)

(d)

Fig. 20. FEM displacements for the stiffened panel: (a) along x-axis (*u*), (b) along y-axis (*v*), (c) along z-axis (*w*), (d) total displacement.
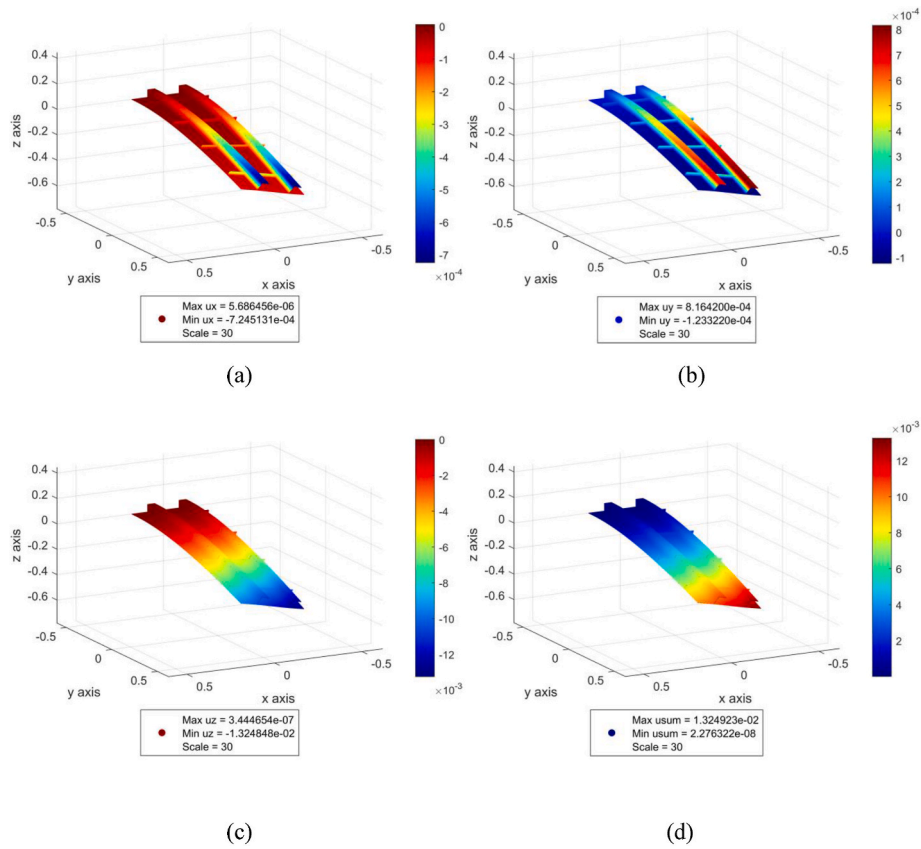
Fig. 21. IgaiMin displacements for the stiffened panel: (a) along x-axis (*u*), (b) along y-axis (*v*), (c) along z-axis (*w*), (d) total displacement.

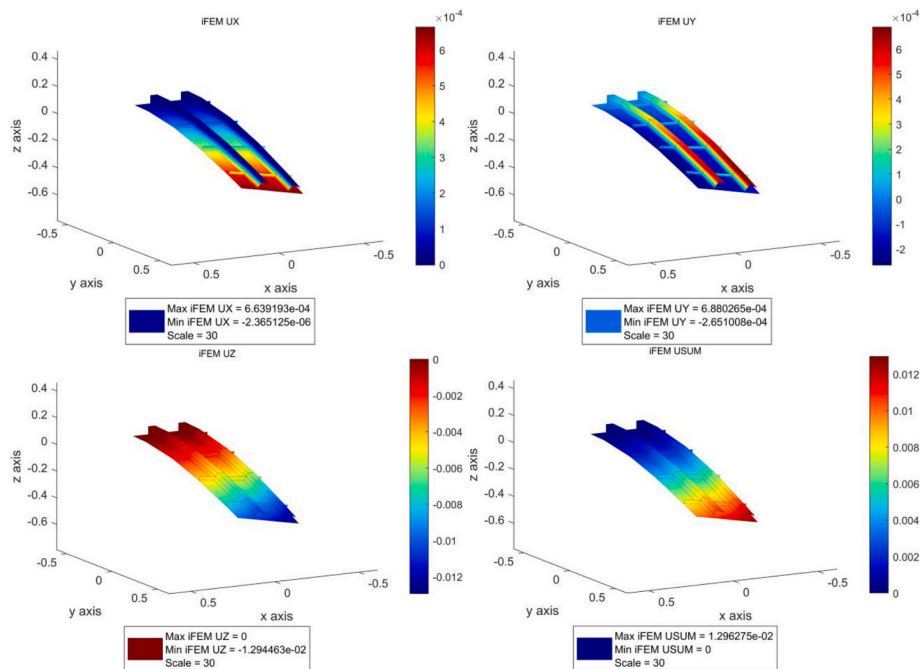**Fig. 22.** IQS4 (Kefal et al., 2016) displacements for the stiffened panel: (a) along x-axis (*u*), (b) along y-axis (*v*), (c) along z-axis (*w*), (d) total displacement.

CRediT authorship contribution statement

Yildirim Dirik: Writing – original draft, Software, Methodology, Conceptualization. **Selda Oterkus:** Writing – review & editing, Supervision, Methodology, Conceptualization. **Erkan Oterkus:** Writing – review & editing, Supervision, Methodology, Conceptualization.

Declaration of competing interest

The authors declare that they have no known competing financial interests or personal relationships that could have appeared to influence the work reported in this paper.

Data availability

Data will be made available on request.

Acknowledgement

We would like to thank Babcock International Group for financial support for the project.

References

Bazilevs, Y., Calo, V.M., Hughes, T.J., Zhang, Y., 2008. Isogeometric fluid-structure interaction: theory, algorithms, and computations. Comput. Mech. 43, 3–37.

Benson, D.J., Bazilevs, Y., Hsu, M.C., Hughes, T., 2010. Isogeometric shell analysis: the Reissner–Mindlin shell. Comput. Methods Appl. Mech. Eng. 199 (5–8), 276–289.

Cerracchio, P., Gherlone, M., Tessler, A., 2015. Real-time displacement monitoring of a composite stiffened panel subjected to mechanical and thermal loads. Meccanica 50, 2487–2496.

Chen, K., Cao, K., Gao, G., Bao, H., 2021. Shape sensing of Timoshenko beam subjected to complex multi-node loads using isogeometric analysis. Measurement: Journal of the International Measurement Confedation 184 (July), 109958.

Cottrell, J.A., Hughes, T.J., Bazilevs, Y., 2009. Isogeometric Analysis: toward Integration of CAD and FEA. John Wiley & Sons.

De Mooij, C., Martinez, M., Benedictus, R., 2019. IFEM benchmark problems for solid elements. Smart Mater. Struct. 28 (6).

Gherlone, M., Cerracchio, P., Mattone, M., Di Sciuva, M., Tessler, A., 2012. Shape sensing of 3D frame structures using an inverse finite element method. Int. J. Solid Struct. 49 (22), 3100–3112.

Hughes, T.J., Cottrell, J.A., Bazilevs, Y., 2005. Isogeometric analysis: CAD, finite elements, NURBS, exact geometry and mesh refinement. Comput. Methods Appl. Mech. Eng. 194 (39–41), 4135–4195.

Kefal, A., Oterkus, E., 2016a. Displacement and stress monitoring of a chemical tanker based on inverse finite element method. Ocean Engineering 112, 33–46.

Kefal, A., Oterkus, E., 2016b. Displacement and stress monitoring of a Panamax containership using inverse finite element method. Ocean Engineering 119, 16–29.

Kefal, A., Oterkus, E., 2017. Shape sensing of aerospace structures by coupling isogeometric analysis and inverse finite element method. In: 58th AIAA/ASCE/AHS/ASC Structures, Structural Dynamics, and Materials Conference, p. 427.

Kefal, A., Oterkus, E., 2020. Isogeometric iFEM analysis of thin shell structures. Sensors 20 (9), 2685.

Kefal, A., Hizir, O., Oterkus, E., 2015. A smart system to determine sensor locations for structural health monitoring of ship structures. In: Proceedings of the 9th International Workshop on Ship and Marine Hydrodynamics, pp. 26–28. Glasgow, UK.

Kefal, A., Oterkus, E., Tessler, A., Spangler, J.L., 2016. A quadrilateral inverse-shell element with drilling degrees of freedom for shape sensing and structural health monitoring. Engineering science and technology, an international journal 19 (3), 1299–1313.

Kefal, A., Mayang, J.B., Oterkus, E., Yildiz, M., 2018a. Three dimensional shape and stress monitoring of bulk carriers based on iFEM methodology. Ocean Engineering 147, 256–267.

Kefal, A., Tessler, A., Oterkus, E., 2018b. An Efficient Inverse Finite Element Method for Shape and Stress Sensing of Laminated Composite and Sandwich Plates and Shells. No. L-20938).

Li, M.Y., Kefal, A., Cerik, B., Oterkus, E., 2019. Structural health monitoring of submarine pressure hull using inverse finite element method. In: Trends in the Analysis and Design of Marine Structures: Proceedings of the 7th International Conference on Marine Structures (MARSTRUCT 2019, Dubrovnik, Croatia, 6-8 May 2019). CRC Press, p. 293.

Li, M., Kefal, A., Oterkus, E., Oterkus, S., 2020a. Structural health monitoring of an offshore wind turbine tower using iFEM methodology. Ocean Engineering 204, 107291.

Li, M., Kefal, A., Cerik, B.C., Oterkus, E., 2020b. Dent damage identification in stiffened cylindrical structures using inverse Finite Element Method. Ocean Engineering 198, 106944.

Li, M., Dirik, Y., Oterkus, E., Oterkus, S., 2023. Shape sensing of NREL 5 MW offshore wind turbine blade using iFEM methodology. Ocean Engineering 273, 114036.

Liu, M., Zhang, X., Song, H., Zhou, S., Zhou, Z., Zhou, W., 2018. Inverse finite element method for reconstruction of deformation in the gantry structure of heavy-duty machine tool using FBG sensors. Sensors 18 (7).

Niu, S., Li, K., Liu, J., Bao, H., 2020. A refined shape sensing method for skin antenna structure based on inverse finite element method. Appl. Sci. 10 (21), 7620.

Oboe, D., Colombo, L., Sbarufatti, C., Giglio, M., 2021. Shape sensing of a complex aeronautical structure with inverse finite element method. Sensors 21 (4), 1388.

Oñate, E., 2013. Structural Analysis with the Finite Element Method. Linear Statics: Volume 2: Beams, Plates and Shells. Springer Science & Business Media.

Papa, U., Russo, S., Lamboglia, A., Del Core, G., Iannuzzo, G., 2017. Health structure monitoring for the design of an innovative UAS fixed wing through inverse finite element method (iFEM). Aero. Sci. Technol. 69, 439–448.

Piegl, L., Tiller, W., 1995. The NURBS Book. Springer-Verlag, New York.

Rogers, D.F., 2001. An Introduction to NURBS: with Historical Perspective. Morgan Kaufmann.

Temizer, I., Wriggers, P., Hughes, T., 2011. Contact treatment in isogeometric analysis with NURBS. Comput. Methods Appl. Mech. Eng. 200 (9–12), 1100–1112.

Tessler, A., Spangler, J.L., 2004. Inverse FEM for full-field reconstruction of elastic deformations in shear deformable plates and shells. In: 2nd European Workshop on Structural Health Monitoring.

Tessler, A., Spangler, J.L., Gherlone, M., Mattone, M., Di Sciuva, M., 2011. Real-time characterization of aerospace structures using onboard strain measurement technologies and inverse finite element method. In: Proceedings of the 8th International Workshop on Structural Health Monitoring, vol. 2. Stanford Univ, Stanford, CA, pp. 981–989.

Wall, W.A., Frenzel, M.A., Cyron, C., 2008. Isogeometric structural shape optimization. Comput. Methods Appl. Mech. Eng. 197 (33–40), 2976–2988.

Wang, J., Ren, L., You, R., Jiang, T., Jia, Z., Wang, G. xin, 2021. Experimental study of pipeline deformation monitoring using the inverse finite element method based on the iBeam3 element. Measurement: Journal of the International Measurement Confederation 184 undefined-undefined.

Xu, M.C., Guedes Soares, C., 2013. Experimental study on the collapse strength of wide stiffened panels. Mar. Struct. 30, 33–62.

Zhao, F., Xu, L., Bao, H., Du, J., 2020. Shape sensing of variable cross-section beam using the inverse finite element method and isogeometric analysis. Measurement 158, 107656.